ФІЗИКО-МАТЕМАТИЧНА ОСВІТА
(PHYSICAL AND MATHEMATICAL EDUCATION)
p-ISSN: 2413-1571, e-ISSN: 2413-158X **2026, 41(2),** **https://doi.org/10.31110/fmo2026.v41i2-03**
UDC: 535.4:004.94:378

ЕКСПЕРИМЕНТАЛЬНА ВІЗУАЛІЗАЦІЯ ТА ЧИСЕЛЬНЕ МОДЕЛЮВАННЯ ДИФРАКЦІЇ ФРАУНГОФЕРА ВІД ВПОРЯДКОВАНИХ І НЕВПОРЯДКОВАНИХ НЕПРОЗОРИХ МІКРОСТРУКТУР ДЛЯ ОСВІТНЬОЇ ПРАКТИКИ

Олексій ВОРОНКІН ✉
Ноттінгемський університет, Велика Британія
Oleksii.Voronkin1@nottingham.ac.uk
https://orcid.org/0000-0003-4088-7147

Сергій ЛУЩИН
Національний університет «Запорізька політехніка», Україна
luschin@zp.edu.ua
https://orcid.org/0000-0003-2135-0520

АНОТАЦІЯ

Формулювання проблеми. *У викладанні дифракції Фраунгофера експериментальні підходи, які чітко демонструють зв'язок між структурами в реальному просторі та їхнім представленням у просторі Фур'є, залишаються обмеженими за доступністю та масштабом застосування. У цій роботі представлено простий, недорогий і наочний метод, що дозволяє студентам спостерігати дифракційні картини та систематично досліджувати вплив виробничих відхилень друкованих оптичних масок.*

Матеріали і методи. *Метод поєднує експериментальну візуалізацію за допомогою бінарних амплітудних масок, надрукованих на прозорій плівці стандартним офісним лазерним принтером, та освітлення напівпровідниковою лазерною указкою, із чисельним моделюванням на основі двовимірного швидкого перетворення Фур'є, реалізованого в Python. Мікроструктури, що охоплюють одномірні дифракційні ґратки, двовимірні періодичні ґратки та структури з базисом (центрована та гексагональна ґратки), а також невпорядковані ансамблі та квазігіперуніформні конфігурації, безпосередньо порівнюються між експериментом і моделюванням. Це порівняння дозволяє детально проаналізувати, як відхилення, зумовлені друком – включно з локальними спотвореннями, помилками позиціонування, розтіканням тонера та частковим злиттям елементів – впливають на дифракційні характеристики.*

Результати. *Результати демонструють, що в періодичних структурах положення максимумів дифракції добре відповідають заданій геометрії, тоді як технологічні недосконалості переважно модулюють інтенсивності, частково відновлюють номінально заборонені порядки та створюють слабкі додаткові максимуми. У невпорядкованих масивах друкованих дисків збільшений ефективний розмір структурних елементів та полідисперсність у надрукованій геометрії призводять до значного згладжування та пригнічення дифракційних кілець вищих порядків, тоді як накладені ближні кореляції створюють характерні особливості, такі як центральне темне кільце. Ці результати ілюструють, як тонкі систематичні та випадкові відхилення від ідеалізованих бінарних амплітудних масок впливають на картини фраунгоферової дифракції, перетворюючи типові артефакти друку на цінний педагогічний інструмент.*

EXPERIMENTAL VISUALIZATION AND NUMERICAL SIMULATION OF FRAUNHOFER DIFFRACTION FROM ORDERED AND DISORDERED OPAQUE MICROSTRUCTURES FOR EDUCATION PRACTICE

Oleksii VORONKIN ✉
University of Nottingham, United Kingdom
Oleksii.Voronkin1@nottingham.ac.uk
https://orcid.org/0000-0003-4088-7147

Sergiy LUSHCHIN
National University Zaporizhzhia Polytechnic, Ukraine
luschin@zp.edu.ua
https://orcid.org/0000-0003-2135-0520

ABSTRACT

Formulation of the Problem. *In teaching Fraunhofer diffraction, experimental approaches that clearly reveal the relationship between real-space structures and their Fourier-space representation remain limited in accessibility and scope. This work presents a simple, low-cost, and visually effective method that enables students to observe diffraction patterns and systematically investigate the influence of fabrication-induced imperfections in printed optical masks.*

Materials and Methods. *The approach combines experimental visualization using binary amplitude masks printed on transparent film with a standard office laser printer and illumination by a low-power semiconductor laser pointer, with numerical simulations based on two-dimensional fast Fourier transforms implemented in Python. Microstructures ranging from one-dimensional gratings to two-dimensional periodic lattices and structures with a basis (centered and honeycomb), as well as disordered ensembles and quasi-hyperuniform configurations, are directly compared between experiment and simulation. This comparison allows detailed analysis of how printer-induced deviations – including local distortions, positioning errors, toner spreading, and partial merging of elements – affect the resulting diffraction features.*

Results. *The results demonstrate that in periodic structures the positions of diffraction maxima closely follow the designed geometry, while fabrication-induced imperfections primarily modulate intensities, partially restore nominally forbidden orders, and generate weak additional maxima. In disordered arrays of printed disks, the increased effective feature size and polydispersity in the printed geometry lead to strong smoothing and suppression of the higher-order diffraction rings, whereas imposed short-range correlations produce characteristic features such as a central dark ring. These findings illustrate how subtle systematic and stochastic deviations from idealized binary amplitude masks influence Fraunhofer diffraction patterns, thereby transforming typical printing artefacts into a valuable pedagogical tool.*

Conclusion. *From an educational perspective, the method provides an affordable, hands-on platform for exploring Fraunhofer diffraction, Fourier optics, reciprocal-space concepts, and statistical correlations. By bridging idealized theoretical models, realistic fabrication limitations, and numerical*

Висновки. *З освітньої точки зору метод забезпечує доступну практичну платформу для вивчення фраунгоферової дифракції, оптики Фур'є, концепцій оберненого простору та статистичних кореляцій. Поєднуючи ідеалізовані теоретичні моделі, реальні обмеження виготовлення та чисельне моделювання, він особливо добре підходить для лабораторних курсів з оптики у вищій освіті.*

КЛЮЧОВІ СЛОВА: *дифракція Фраунгофера; експериментальна візуалізація; чисельне моделювання; оптика Фур'є; впорядковані та невпорядковані системи; лазерний друк мікроструктур.*

ДЛЯ ЦИТУВАННЯ: Voronkin O., Lushchin S. Experimental visualization and numerical simulation of fraunhofer diffraction from ordered and disordered opaque microstructures for education practice. *Фізико-математична освіта*, 2026. Том 41. № 2. С. 28-45. https://doi.org/10.31110/fmo2026.v41i2-03.

simulation, it is particularly well suited for undergraduate laboratory courses in wave optics.

KEYWORDS: *Fraunhofer diffraction; experimental visualization; numerical simulation; Fourier optics; ordered and disordered systems; laser printing of microstructures.*

FOR CITATION: Voronkin, O., & Lushchin, S. (2026). Experimental visualization and numerical simulation of fraunhofer diffraction from ordered and disordered opaque microstructures for education practice. *Physical and Mathematical Education*, *41*(2), 28-45. https://doi.org/10.31110/fmo2026.v41i2-03.

INTRODUCTION

Problem statement. Fraunhofer diffraction remains one of the most visually striking and pedagogically valuable phenomena in wave optics. It provides a direct experimental visualization of how the size, shape, and spatial arrangement of obstacles affect the resulting far-field pattern, making diffraction experiments powerful tools for instructional physics courses and educational visualizations of ordered and disordered optical structures. At the same time, there remains a need for accessible experimental approaches that facilitate students' understanding of diffraction from a variety of ensembles and clearly demonstrate the correspondence between real and reciprocal space.

This correspondence between object geometry and the far-field diffraction pattern is illustrated by well-known atmospheric diffraction phenomena, such as coronae around the Sun and Moon, whose ring structure is governed by Fraunhofer diffraction from nearly monodisperse cloud droplets (Cowley et al., 2005).

Literature review. Similar phenomena can be reproduced in the classroom using controlled scatterer ensembles. High-resolution laser printers enable sufficiently regular microstructures that yield diffraction patterns comparable to optical gratings (Brady & Boardman, 1995; Van Hook, 2007). The resulting patterns resemble Laue X-ray diffraction photographs, illustrating the connection between crystallography and optical diffraction. Optical Laue diffraction has been demonstrated on two-dimensional photonic structures with hexagonal packing (Naimi, 2013), while modern approaches employ computer-generated masks on spatial light modulators, forming complex structures in real time and allowing instantaneous observation of their Fourier images (Huang et al., 2012). Diffraction patterns for all five two-dimensional Bravais lattices have also been reproduced using pairs of linear gratings (Tsutaoka et al., 2014).

The pedagogical value of such experiments is enhanced when integrated with numerical simulation. Direct comparison of observed patterns with computed Fourier transforms allows students to trace the correspondence between real-space geometry and reciprocal-space representation (Peinado et al., 2012) and explore the effects of periodicity, defects, statistical fluctuations, and scatterer size on the far-field structure.

Particular interest arises when the scatterers consist of ensembles of opaque disks with disordered or correlated placements. Each disk acts as a two-dimensional optical analog of a spherical microparticle, so that the far-field diffraction pattern provides a vivid model for powder X-ray diffraction, light scattering from colloids, and two-dimensional particle arrays.

The progression from ordered structures (discrete Bragg peaks) through Poisson-distributed configurations to hyperuniform ensembles (suppressing small-angle scattering) makes the evolution of the structure factor visually evident. However, despite these advances, existing studies primarily focus on ordered periodic structures or isolated demonstrations, whereas systematic and accessible experimental approaches for illustrating diffraction from disordered and correlated ensembles – particularly in combination with quantitative analysis of fabricated masks produced by laser printing – remain insufficiently developed for instructional use.

The purpose of the study. The purpose of this study is to develop and present an integrated method combining printed binary masks with numerical simulation for instructional visualization of Fraunhofer diffraction, taking into account printer resolution, pixelation effects, and fabrication-induced variations.

This framework enables systematic exploration of diffraction patterns across ordered gratings, random Poisson distributions, Poisson Disk Sampling distributions, and hyperuniform ensembles (Torquato & Stillinger, 2003; Torquato, 2018). Each ensemble produces a distinctive far-field "fingerprint," and comparison between experiment and simulation is restricted to geometry-based descriptors of the diffraction pattern. These include the radial positions of intensity extrema in ring-like structures and the inter-spot distances in discrete patterns, without using absolute or relative intensity values.

By integrating numerical simulation with experimental visualizations using digital printing and accessible laser optics, this approach provides students with an engaging and effective means to visualize and explore Fourier optics, concepts of statistical physics, and the relationship between real and reciprocal space.

METHODS OF THE RESEARCH

Generation of microstructures. The microstructures were programmatically generated using Python. All masks were designed for printing on OHP laser-printer transparency film (A4 format) at a resolution of 1200 × 1200 dpi using a Brother HL-L2400DW printer. The physical dimensions of structural elements were specified in micrometers and converted to pixels within the Python scripts according to the relation (1).

$$1\ px = \frac{1\ inch}{1200\ dpi} \approx 21.17\ \mu m. \quad (1)$$

The minimum practical feature size was chosen to be 80–84 μm, corresponding to approximately 4 pixels according to equation (1). This size ensures the formation of fully opaque regions with adequate and uniform toner thickness.

All masks were physically printed on premium 100 μm-thick laser-printer transparency film using the HQ1200 / Graphics mode.

Printing considerations. Microscopic inspection of the printed masks reveals several non-idealities inherent to laser-printing-based fabrication, including edge roughness, limited lateral toner spreading, and local distortions in regions with closely spaced elements. Similar fabrication-induced feature broadening and partial merging effects have been reported in studies of laser-printed photomasks and toner-based pattern transfer (Easley et al., 2009; Ghosh et al., 2019).

From an educational perspective, such fabrication-induced variations illustrate the interplay between theoretical design, numerical simulation, and experimental implementation, highlighting how practical constraints affect observed optical diffraction patterns. In each visualization, these detected defects are considered, and their influence on the resulting diffraction pattern is systematically analyzed to demonstrate how deviations from ideal geometry affect both periodic and disordered ensembles.

Experimental setup and Fraunhofer conditions. In the experiment, a standard semiconductor laser pointer (λ = 0.532 μm, output power < 5 mW, Class II) was employed. Basic laser-safety precautions appropriate for Class II devices were observed throughout the setup.

The laser beam was directed perpendicular to the surface of the transparency film carrying the printed microstructure. The distance from the laser pointer to the film was h = 0.20 m. The diffraction pattern was observed on a screen placed at a distance z = 6.50 m from the mask, a separation that simultaneously satisfies two independent Fraunhofer-condition criteria.

The first condition governs the applicability of the Fraunhofer approximation and is determined by the effective lateral extent of the illuminated region on the mask (Born & Wolf, 1999; Guenther, 2020; Hecht, 2017). The standard criterion is expressed as

$$z \gg R^2/4\pi\lambda, \quad (2)$$

where R is the radius of the illuminated region on the mask, defined as half the transverse dimension of the microstructured film section within which the laser beam produces significant illumination.

For the present experimental visualization, the radius of the illuminated region was R = 1 mm, yielding the requirement $z \gg 0.15$ m according to equation (2). A more rigorous estimate, based on the maximum quadratic phase shift, gives $z \gg \pi R^2/\lambda \approx 5.9$ m (Rayleigh range). The chosen screen distance of z = 6.5 m comfortably exceeds this stricter threshold, fully satisfying the Fraunhofer (far-field) condition and ensuring sharp, well-defined diffraction patterns.

The second condition pertains to the characteristic size of an individual opaque element (line, disk, or square). For the diffraction pattern of a single obstacle to conform rigorously to the classical Fraunhofer expressions, the linear dimensions of the element are typically chosen to substantially exceed the wavelength (Bertero et al., 1985). In the present structures, this dimension ranges from 80 to 84 μm – more than 150 times the wavelength of the radiation (λ = 0.532 μm). This substantial ratio ensures excellent reproducibility of the single-element form factor and validates the quantitative interpretation of the observed diffraction patterns.

Image acquisition and processing. Diffraction patterns were recorded using a Nikon D850 digital single-lens reflex camera equipped with a Nikon AF-S VR Micro-NIKKOR 105 mm f/2.8G IF-ED lens. The camera was mounted on a tripod to eliminate motion blur during long exposures under low-light conditions.

Experimental images were converted to grayscale and calibrated in spatial coordinates using a known pixel-to-length ratio. For visualization and comparison with simulations, intensity values were globally normalized by their maximum value, yielding dimensionless intensities in the range [0, 1].

Optical micrographs of the fabricated masks were acquired using a Leica M205 stereomicroscope. These micrographs were further analyzed using ImageJ software (Schneider et al., 2012) to measure geometric parameters, including equivalent element diameters (based on area), shape (aspect ratios), halo size, lattice periods in periodic arrays, and characteristic distances such as the minimum center-to-center spacing in disordered (e.g., Poisson Disk Sampling) ensembles. These measurements provided quantitative information on fabrication-induced variations, enabling comparison with the nominal designed values and supporting interpretation of the corresponding diffraction patterns.

Numerical simulation. Diffraction patterns were numerically simulated using the two-dimensional fast Fourier transform (2D FFT) method on a uniform grid of 4096 × 4096 pixels, which balances spatial resolution and computational efficiency. The chosen discretization provides 45–69 grid points across each element diameter, ensuring accurate representation of shapes and relative positions for all configurations, including one- and two-dimensional gratings, centered and primitive unit cells, hexagonal and honeycomb lattices, as well as random (uncorrelated) and hyperuniform ensembles.

All masks were generated as binary images representing opaque elements on a transparent background. The physical printed masks have coarser resolution (~4 pixels per element) with widened and irregular edges, which are not fully captured in the numerical model. In the simulation, a slight Gaussian smoothing (σ ≈ 1.5 pixels of the computational grid) was applied to the element boundaries solely to avoid unrealistically sharp edges introduced by the discrete numerical grid. This smoothing does not alter the nominal element size or the overall lattice geometry, but facilitates a more stable and visually realistic representation of diffraction features. Measured fabrication-induced variations, such as size fluctuations, edge roughness, and spacing deviations identified via ImageJ analysis, were generally taken into account qualitatively in interpreting the simulated diffraction patterns; in cases where these variations noticeably affected the pattern, the experimentally measured geometries were used directly in the numerical simulation.

The illumination was simulated by a Gaussian beam with a wavelength of λ = 0.532 μm, whose intensity distribution in the aperture plane is described by equation (3), which is equivalent to the form presented in (Siegman, 1986).

$$I_{beam}(r) = e^{-\frac{2r^2}{\omega_0^2}}, \quad (3)$$

where r is the distance from the beam center, ω_0 = 1 mm is the beam waist radius (defined at the $1/e^2$ intensity level), corresponding to the experimentally used illuminated region.

The resulting complex field in the mask plane was propagated to the far field using a 2D FFT, yielding the Fraunhofer diffraction pattern that can be directly compared with experimental observations.

All intensity maps are presented in normalized form for visualization due to the high dynamic range of both experimental and simulated data. Experimental images are normalized with respect to the maximum recorded intensity, while simulated intensity distributions are given in normalized units.

All simulated diffraction patterns of periodic structures (e.g., gratings) are shown using a linear intensity scale with optional saturation, unless otherwise stated. For ring-like diffraction patterns (e.g., Airy-like or disorder-induced circular patterns), nonlinear tone mapping is applied only to simulated images for visualization purposes to enhance weak diffraction features, such as higher-order rings. These processing steps preserve the spatial structure of the diffraction patterns and do not affect the positions, symmetry, or locations of intensity maxima; all such cases are explicitly indicated in the corresponding figure captions.

Comparison between experimental diffraction patterns and numerical simulations is performed primarily based on spatial characteristics (positions and radii of maxima and rings), since the possible nonlinear response of the imaging system (CMOS camera, Nikon D850), limited dynamic range, and variations in exposure conditions prevent reliable direct comparison of absolute intensities. The main validation of the fabricated masks was performed using optical microscopy and quantitative ImageJ analysis.

All data, including experimental diffraction photographs, optical microscopy images of fabricated masks, numerical simulations, Python scripts for data processing and visualization, and PNG files of masks used for printing, are available in an open-access repository (Voronkin & Lushchin, 2026).

RESULTS OF RESEARCH

1. Fraunhofer diffraction on a one-dimensional grating. Fraunhofer diffraction on a one-dimensional grating is considered. As a first experimental visualization, diffraction from a one-dimensional amplitude grating consisting of vertical opaque stripes is presented. The grating was first designed as a digital amplitude mask and subsequently fabricated by laser printing on a transparent film. The structure is characterized by an opaque stripe width a = 84 μm (≈4 pixels), grating period d = 252 μm (≈12 pixels), and a calculated filling factor η ≈ 0.33.

In practice, the printed grating exhibits slight imperfections: the effective stripe width varies due to the granular toner structure, edge roughness, and local spreading. Within the analyzed area of approximately 2.9 × 10^6 μm², six opaque vertical stripes were identified. ImageJ analysis (see Appendix A, Figure A1a) shows that:

- Average period 256.8 ± 6.8 μm (nominal 252 μm, relative deviation +1.9 %);
- Stripe width 99.6 ± 17.0 μm (nominal 84 μm, relative deviation +18.6 %);
- filling factor η ≈ 0.39.

The relatively large uncertainty in the stripe width arises from irregular and wavy boundaries, accompanied by a diffuse halo, with the width varying between 5 and 11 μm across different regions, caused by inhomogeneous toner deposition. As a result, the stripe width should be understood as an effective value, since the exact position of the edge depends on the chosen intensity threshold.

Under normal laser illumination, a classical diffraction pattern consisting of a central maximum and symmetrically spaced higher-order maxima is observed. However, deviations in the visibility and relative prominence of diffraction orders are observed qualitatively when compared with the idealized model, while no quantitative intensity comparison is performed.

Figure 1 compares the experimental diffraction pattern (A) with the numerical simulation for the nominal grating geometry (B).

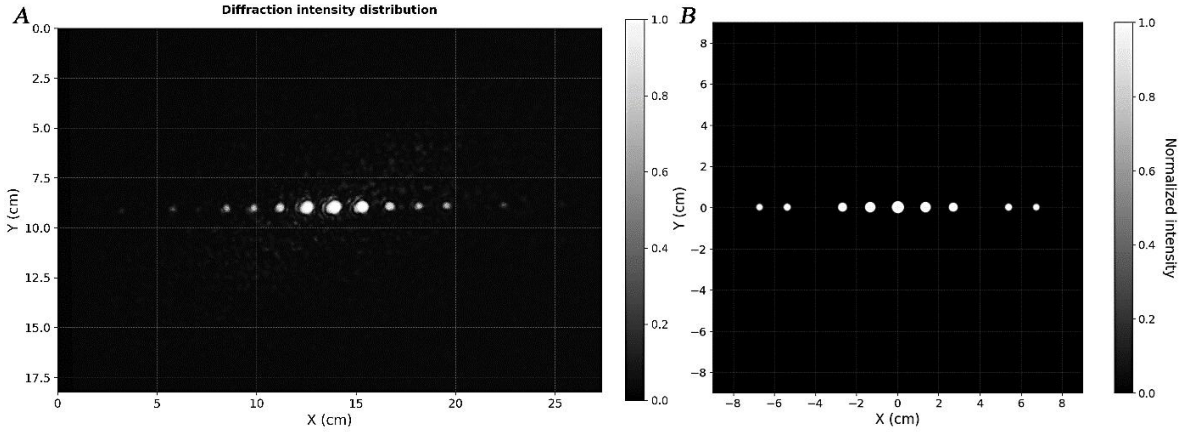

Fig. 1. Diffraction pattern obtained for a one-dimensional amplitude vertical grating: A – experimental diffraction pattern for the printed grating; B – numerical simulation for the nominal grating geometry (d = 252 μm, a = 84 μm). The simulation is shown using a linear intensity scale with normalization and a display-only intensity clipping threshold I_{sat} = 0.002

Source: author's own work

An additional simulation using experimentally determined effective parameters is presented in Figure 2. This allows direct assessment of the influence of fabrication induced deviations.

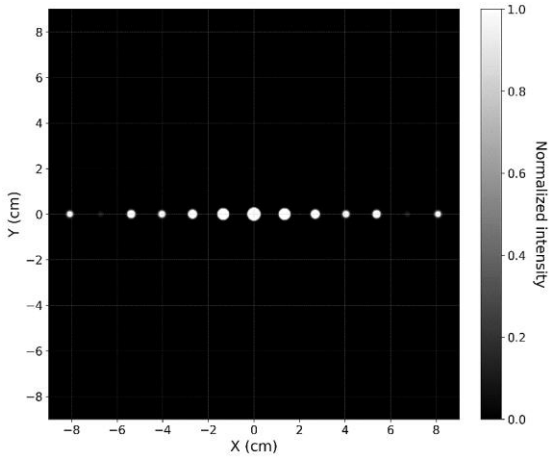

Fig. 2. Numerical simulation of diffraction from the same grating using experimentally determined effective parameters (d ≈ 257 µm, a ≈ 100 µm). Linear normalization and display-only clipping (I_{sat} = 0.002) were applied following the same procedure as in Figure 1

Source: author's own work

For the nominal grating geometry, the ratio d/a = 3 satisfies the condition for missing diffraction orders, whereby the maxima of the grating interference function coincide with the zeros of the single-slit diffraction envelope, resulting in the suppression of every third diffraction order. In the experimental pattern, the third diffraction order is partially restored due to effective stripe broadening and local edge variations, which reduce the ideal suppression predicted for a uniform grating.

In the experimental pattern, however, the ratio d/a≈2.58 deviates from this condition. As a result, exact cancellation no longer occurs, and the missing orders are replaced by strongly attenuated diffraction maxima. The third-order maximum is partially restored due to effective stripe broadening and local edge variations.

The increased filling factor (η≈0.39) leads to a narrowing of the diffraction envelope, causing enhanced suppression of higher diffraction orders. In particular, the fifth-order maximum is expected to be strongly attenuated, as it lies close to the second minimum of the envelope function.

The following subsections consider structures composed of isolated elements, represented as opaque disks. These elements serve as simplified models of discrete scatterers or particle projections. Such a representation enables a direct correspondence between the real-space arrangement of elements and the resulting diffraction pattern, providing a consistent framework for both numerical simulations and experimental visualizations of spatial correlations.

2. Fraunhofer diffraction by a two-dimensional periodic grating formed by a regular array of opaque disks. In this subsection, we consider Fraunhofer diffraction from a two-dimensional amplitude grating consisting of a square array of opaque disks. The structure was first designed as a digital amplitude mask, comprising disks of diameter D = 84 µm (4 pixels at 1200 dpi), arranged on a square lattice with period $d_x = d_y = d$ = 169 µm (8 pixels). The physical mask was then fabricated by laser printing on a transparent film.

For a periodic array of identical objects, the disk shape defines the envelope of the diffraction pattern, while the lattice periodicity determines the positions of the maxima. In the small-angle approximation, the coordinates of the maxima on the screen located at a distance z from the mask with the diffraction grating are given by the expressions:

$$x_{m,n} \approx z\frac{m\lambda}{d_x},\ y_{m,n} \approx z\frac{n\lambda}{d_y}. \quad (4)$$

For a square grating ($d_x = d_y = d$), the diffraction pattern consists of a regular two-dimensional grid of bright spots, corresponding to the index pairs (m, n). The central maximum corresponds to the (0, 0) order; the nearest maxima to (±1, 0) and (0, ±1); and the diagonal ones to (±1, ±1). This structure is a direct representation of the reciprocal lattice.

From the above expressions, a simple relationship follows between the grating period and the distance between adjacent diffraction maxima relative to the center:

$$\Delta x_1 = x_{1,0} \approx \frac{z\lambda}{d_x};\ \Delta y_1 = y_{0,1} \approx \frac{z\lambda}{d_y}. \quad (5)$$

To improve experimental accuracy, the lattice period can be estimated by averaging values obtained from multiple diffraction orders:

$$\overline{d_x} \approx \left\langle z\frac{m\lambda}{x_{m,0}}\right\rangle_{m=1,2},\ \overline{d_y} \approx \left\langle z\frac{n\lambda}{y_{0,n}}\right\rangle_{n=1,2}. \quad (6)$$

This approach allows for reducing the impact of experimental errors and enhances the robustness of the result.

A quantitative characterization of the fabricated mask (see Appendix A, Figure A1b) was performed using ImageJ. The spatial calibration was based on a 250 µm reference scale. Within an analyzed area of approximately 2.9 × 10^6 µm², 93 disks were identified. The measured parameters are:

- vertical period: 177.4 ± 7.4 µm (nominal 169 µm, relative deviation +4.97 %);

- horizontal period: 176.8 ± 18.7 μm (nominal 169 μm, relative deviation +4.62 %);
- equivalent disk diameter: D = 83.3 ± 36.3 μm (nominal 84 μm);
- aspect ratio AR = 1.3 ± 0.3.

The disk diameter was defined via the equivalent-area method. The relatively large uncertainty is attributed to irregular disk boundaries, including edge roughness and a diffuse halo caused by non-uniform toner deposition.

Figure 3 compares the experimentally observed diffraction pattern with a numerical simulation based on the measured parameters. Despite minor deviations in disk shape and a ∼5 % increase in the lattice period, the maxima positions agree well with theoretical predictions, whereas intensity distributions are not compared quantitatively due to experimental and visualization limitations.

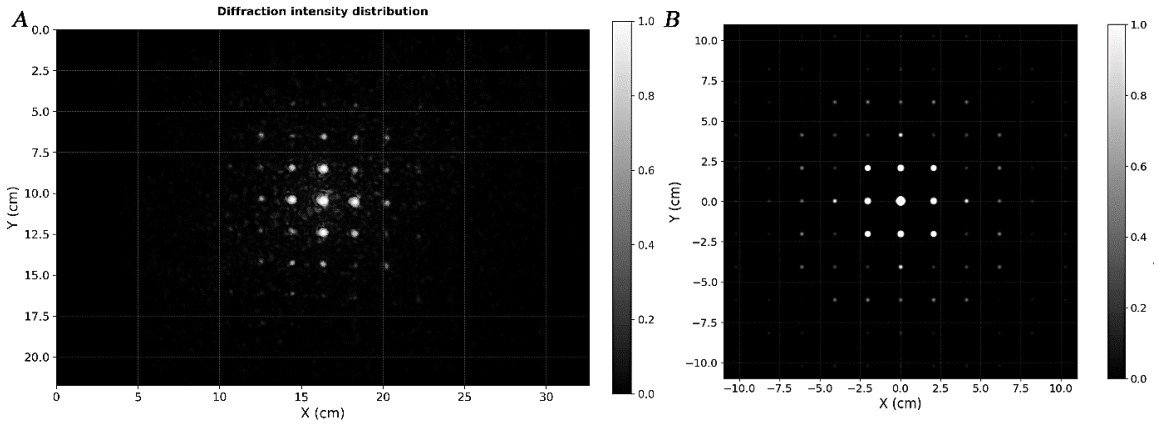

Fig. 3. Comparison of diffraction patterns: A – experimental pattern on the screen; B – numerical simulation of Fraunhofer diffraction (D = 84 μm, d = 169 μm). Linear normalization and display-only clipping (I_{sat} = 0.002) were applied only to the simulated image, following the same procedure as in Figure 1

Source: author's own work

From a pedagogical perspective, this example highlights the separation between the roles of lattice periodicity and single-element geometry in diffraction: the positions of the maxima are determined by the global periodic structure, whereas their intensities are influenced by the shape of individual elements.

3. Fraunhofer diffraction on a periodic square grating with additional central disks. In this visualization, a modified two-dimensional amplitude structure is presented, corresponding to a square periodic grating with additional elements located at the centers of the unit cells. Such a structure corresponds to a centered square lattice (c-centered square lattice). It can be represented as the superposition of two interpenetrating square sublattices: sublattice A, consisting of disks positioned at the nodes of a square grid, and sublattice B, comprising identical disks but shifted by the vector $\mathbf{\Delta} = (d/2, d/2)$.

In the digital design, the base structure consists of opaque disks with a diameter of D = 80 μm (≈4 pixels), positioned at the nodes of a square grid with a period of d = 300 μm (≈14 pixels). An additional disk of the same diameter is placed at the center of each unit cell, shifted by the vector $\mathbf{\Delta}$.

The period of the primary sublattice A determines the spacing between adjacent maxima on the screen: $\Delta x = \Delta y \approx 1.15$ cm (see equation (5)). Sublattice B produces a sparser grid of maxima, yielding $\Delta x = \Delta y \approx 2.31$ cm. The offset of sublattice B relative to A gives rise to a structure factor – a phase factor that modulates the intensity of the diffraction orders.

Although the diffraction pattern is convenient for visual comparison in (x, y) coordinates, a rigorous analysis of all diffraction orders requires the use of reciprocal lattice vectors $\boldsymbol{b_1}$ and $\boldsymbol{b_2}$.

Each maximum on the screen corresponds to a reciprocal lattice vector $\boldsymbol{G}_{mn}$:

$$\boldsymbol{G}_{mn} = m\boldsymbol{b}_1 + n\boldsymbol{b}_2,\ m, n \in \mathbb{Z} \tag{7}$$

where $\boldsymbol{b}_1$ is the first basis vector of the reciprocal lattice along the x-axis, $\boldsymbol{b}_2$ is the second basis vector of the reciprocal lattice along the y-axis.

These indices (m, n) determine whether a given diffraction order will be bright or suppressed in accordance with the structure factor of the centered lattice. The introduction of the reciprocal lattice provides a natural framework for describing the alternation of allowed and forbidden maxima (the condition requiring even $m + n$) and for correctly interpreting the observed pattern, including the weak intermediate orders and their phase relationships.

The phase factor induced by the shift vector $\mathbf{\Delta}$ is given by

$$e^{i\boldsymbol{G}_{mn}\cdot\mathbf{\Delta}} = e^{i\pi(m+n)}. \tag{8}$$

Consequently, the structure factor of the centered lattice is then:

$$S(m,n) = 1 + e^{i\pi(m+n)}, \tag{9}$$

which yields bright maxima (S = 2) when $m + n$ is even and suppressed diffraction orders (S = 0) when $m + n$ is odd.

It is precisely the alternation of allowed and forbidden diffraction orders that gives rise to the characteristic appearance of the diffraction pattern. In practice, perfect suppression of odd orders is not observed experimentally, which is attributable to residual intensity from nearly suppressed orders, side lobes, the finite number of elements in the mask, as well as fabrication-specific factors.

Direct inspection of the printed mask (see Appendix A, Figure A1c) reveals deviations from the nominal geometry. ImageJ-based analysis identified 48 disks within an area of 2.9×10^6 μm^2. The measured parameters are:

- horizontal period 315.6 ± 3.5 μm (nominal 300 μm, relative deviation +5.2 %);
- vertical period 330.0 ± 21.3 μm (nominal 300 μm, relative deviation +10.0 %);
- aspect ratio AR = 1.1 ± 0.1;
- disk diameter D = 151.0 ± 7.0 μm (nominal 80 μm, relative deviation +88.8 %).

Unlike the smaller-period structures, this configuration exhibits well-defined disk edges without pronounced halo formation; however, the effective disk diameter is significantly increased. This unusually large deviation is observed only for this mask and is likely related to printer-specific rasterization or exposure algorithms at larger feature spacing (>300 μm), in addition to toner spreading and edge broadening effects.

Figure 4 compares the experimental diffraction pattern with the numerical simulation based on nominal parameters.

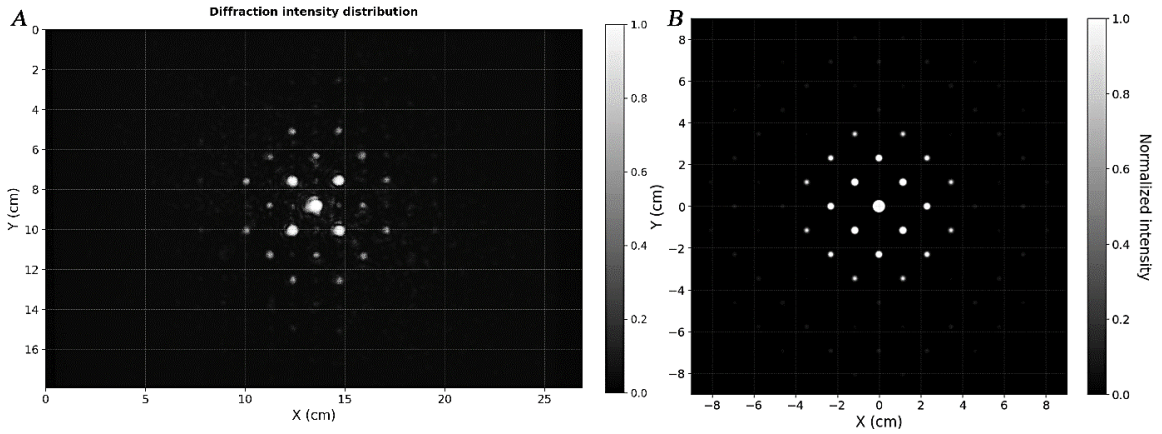

Fig. 4. Comparison of diffraction patterns: A – experimental pattern on the screen; B – numerical simulation (D = 80 μm, d = 300 μm). Linear normalization and display-only clipping (I_{sat} = 0.002) were applied only to the simulated image, following the same procedure as in Figure 1

Source: author's own work

The experimental pattern exhibits weak, barely visible residual odd-order maxima near the central region, which are absent in the ideal case. These arise from incomplete destructive interference due to deviations from perfect lattice symmetry.

Several factors contribute to this effect. First, anisotropy in the lattice periods (315.6 μm vs 330.0 μm) distorts the reciprocal lattice, leading to imperfect phase matching for destructive interference. Second, measured positional deviations of disk centers (on the order of ±3.5 μm in x and ±21.3 μm in y) further reduce the efficiency of suppression of these orders.

Students can directly observe how deviations from ideal symmetry, including size variations and lattice anisotropy, affect interference conditions and lead to incomplete extinction of nominally forbidden orders. These disk position deviations can arise from mechanical noise in film feeding, laser positioning accuracy, local toner deposition variations, or microscopic vibrations of the film. This provides another clear and accessible illustration of how real structural imperfections modify diffraction patterns, bridging the gap between idealized theoretical models and experimentally realizable structures.

4. Diffraction by a two-dimensional hexagonal grating of opaque disks. In this visualization, a two-dimensional structure composed of identical opaque circular disks arranged at the nodes of a hexagonal lattice is employed. Each disk in this lattice has six equivalent nearest neighbors, forming the classic triangular packing arrangement.

The structure was designed as a digital amplitude mask using the Python Imaging Library (PIL) and subsequently fabricated by laser printing on a transparent film. The disks in the design had a nominal diameter D = 84 μm (≈4 pixels at 1200 dpi).

The grating parameters were selected by minimizing structural anisotropy. The algorithm scanned possible values of the horizontal period d_x (restricted to even pixel values to ensure integer row offsets) and computed the corresponding vertical period from the hexagonal relation $d_y = d_x\sqrt{3}/2$, rounded to the nearest integer number of pixels. Anisotropy was quantified as the difference between distances to horizontal and diagonal nearest neighbors.

The optimal configuration was found to be: horizontal period d_x = 8 pixel (169 μm), vertical period d_y = 7 pixel (148 μm), and an offset of 4 pixel (84.5 μm) for odd-numbered rows. This yields a quasi-hexagonal grating with a nearest-neighbor distance of approximately 169 μm.

At the design stage, rounding of d_y introduces a residual anisotropy of ≈ 0.78 %, with nearest-neighbor distances ranging from 3.9 to 4.7 pixels and a lattice angle of 60.26^0 instead of the ideal 60^0. However, the experimentally fabricated mask exhibits additional and more pronounced deviations arising from the printing process, which further distort the lattice geometry beyond this intrinsic discretization limit.

Figure 5 presents a comparison between the experimental diffraction pattern and the result of numerical simulation performed in Python.

For the numerical simulation, an ideal hexagonal lattice was used, with disk centers defined with floating-point precision (64-bit), avoiding pixel-grid rounding. The disk diameter was D = 84 μm, and the nearest-neighbor distance was 169 μm. The vertical period was computed with machine precision, ensuring exact hexagonal symmetry.

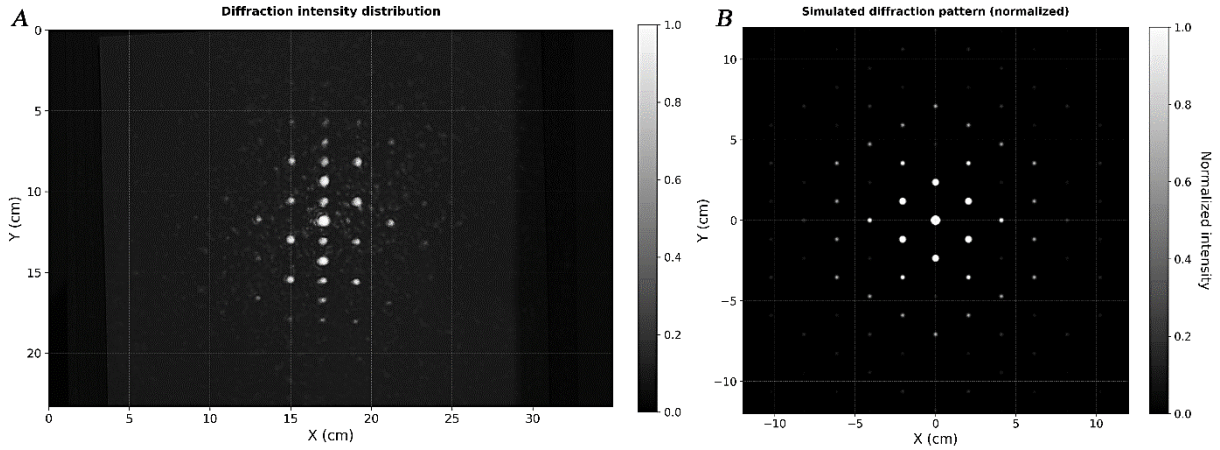

Fig. 5. Comparison of diffraction patterns: A – experimental pattern; B – numerical simulation of Fraunhofer diffraction for ideal grating geometry (D = 84 μm, nearest-neighbor spacing a = 169 μm). Linear normalization and display-only clipping (I_{sat} = 0.002) were applied only to the simulated image, following the same procedure as in Figure 1

Source: author's own work

In the experimental diffraction pattern, the central vertical axis exhibits primary maxima with spacing $\Delta y \approx 2.5$ cm (Figure 5A). In addition, weaker secondary maxima appear at half-spacing $\Delta y/2 \approx 1.2$ cm. These peaks are absent in the ideal simulation (Figure 5B), indicating a deviation from perfect hexagonal periodicity.

Quantitative analysis of the printed mask (see Appendix A, Figure A1d) using ImageJ on a representative region ($\approx 2.9 \times 10^6$ μm^2, 95 disks) reveals:

- D = 91.0 ± 9.3 μm (nominal 84 μm, relative deviation +8.3 %), halo width ≈ 8–10 μm;
- AR = 1.1 ± 0.1;
- d_x = 177.4 ± 15.1 μm (nominal 169 μm, relative deviation +5.0 %);
- d_y = 167.8 ± 18.4 μm (nominal 148 μm, relative deviation +13.4 %);
- nearest-neighbor distance a = 179.0 ± 13.5 μm (nominal 169 μm, relative deviation +5.9 %).

The ratio $d_x/d_y \approx 1.06$ deviates from the ideal geometric relation for a hexagonal lattice $2/\sqrt{3} \approx 1.155$, indicating a distortion of lattice symmetry.

However, a more detailed analysis reveals that this is not a simple uniform distortion. The inter-row spacings exhibit locally alternating shorter (≈154 μm) and longer (≈195 μm) values, forming a periodic short–long modulation. The average spacing ($d_{y,\text{eff}} \approx 174.5$ μm) is close to the measured d_y, but the alternation breaks translational symmetry along the vertical direction and introduces an additional spatial frequency corresponding to a doubled period.

In reciprocal space, this modulation produces additional diffraction maxima at half the primary spacing ($\Delta y/2 \approx \lambda \cdot z / (2 \cdot d_{y,\text{eff}}) \approx 0.99$ cm).

Figure 6 shows a numerical simulation incorporating this vertical modulation ($d_x \approx 178$ μm, $d_{y,\text{short}} \approx 154$ μm, $d_{y,\text{long}} \approx 195$ μm). Simulation also predicts a weaker secondary component at approximately 0.99 cm, in addition to the $\Delta y/2 \approx 1.2$ cm peak. However, this feature is not clearly resolved in the experimental diffraction pattern, where only the 1.2 cm component is consistently observed. This suggests that the real fabrication-induced modulation deviates from an ideal periodic perturbation, likely exhibiting a non-ideal modulation profile and local structural variations that selectively enhance specific components while suppressing others.

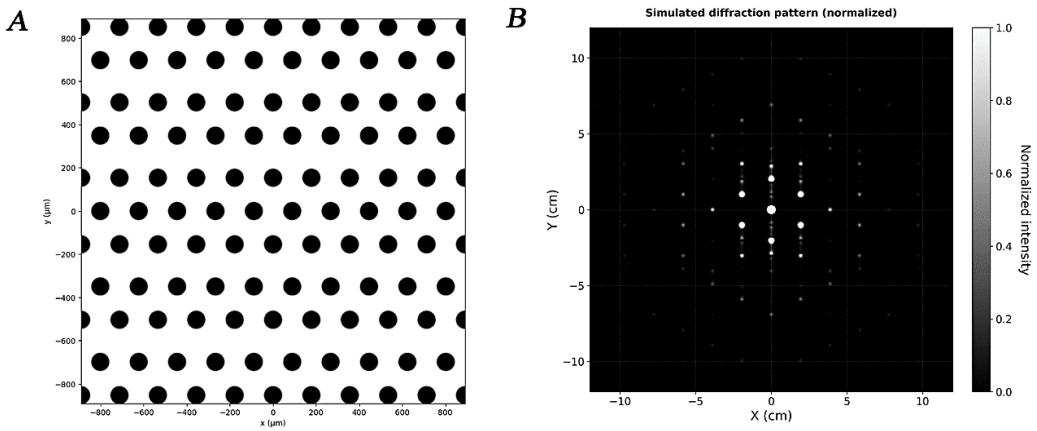

Fig. 6. Numerical simulation of Fraunhofer diffraction for a hexagonal disk array with a modulated vertical period: A – digital amplitude mask with alternating inter-row spacing (D = 84 μm, d_x = 178 μm, $d_{y,\text{short}}$ = 154 μm, $d_{y,\text{long}}$ = 195 μm); B – corresponding simulated diffraction pattern. Linear normalization and display-only clipping (I_{sat} = 0.002) were applied only to the simulated image, following the same procedure as in Figure 1

Source: author's own work

These results demonstrate that the observed anomalies originate primarily from a systematic vertical modulation of the lattice (likely a printing-induced positioning artifact or the printer's internal rasterization algorithm), rather than from random size variations or uniform lattice distortion. From a pedagogical perspective, this example highlights how subtle real-space periodic modulations give rise to additional features in reciprocal space, providing a clear link between fabrication imperfections and diffraction patterns.

5. Diffraction by a two-dimensional honeycomb grating. The honeycomb lattice is a two-dimensional periodic structure with a two-atom basis, composed of two mutually displaced sublattices A and B. Each sublattice individually forms a triangular lattice; however, their relative offset results in each site having exactly three nearest neighbors. This geometry forms a network of regular hexagons and is characteristic of important physical systems such as graphene.

The structure was first designed as a digital amplitude mask and subsequently fabricated by laser printing on a transparent film. The disk positions were generated programmatically based on hexagonal geometry. The construction algorithm included:

- Generation of a grid of hexagon centers with a horizontal period of $d_x = 3a/2 = 253.5$ μm (spacing between adjacent columns of centers) and a vertical period of $d_y = a\sqrt{3} \approx 292.7$μm (spacing between centers within the same column).
- Downward vertical offset of every odd-numbered column of centers by $d_y/2 \approx 146.4$ μm to achieve hexagonal packing of the hexagon centers.
- Placement of six opaque disks of diameter $D = 84$ μm at the vertices of each hexagon, located at a distance $a = 169$ μm from the hexagon center and at angular positions 0^0, 60^0, 120^0, 180^0, 240^0, and 300^0.

The coordinates of the disk centers were computed with floating-point precision and subsequently rounded to the nearest pixel at 1200 dpi resolution. At this resolution, the disk diameter corresponds to approximately 4 pixels, while the grating parameter $a \approx 8$ pixels. The rounding error for the center coordinates is ±10.6 μm (half a pixel), resulting in a relative error of approximately 6 % of the disk diameter and approximately 3 % of the grating parameter a.

Each disk belongs to three adjacent hexagons, establishing a honeycomb topology with three nearest neighbors per site at a distance a. The centers of the hexagons remain empty (transparent).

Figure 7 presents a comparison between the experimental diffraction pattern and the result of numerical simulation for ideal honeycomb grating geometry.

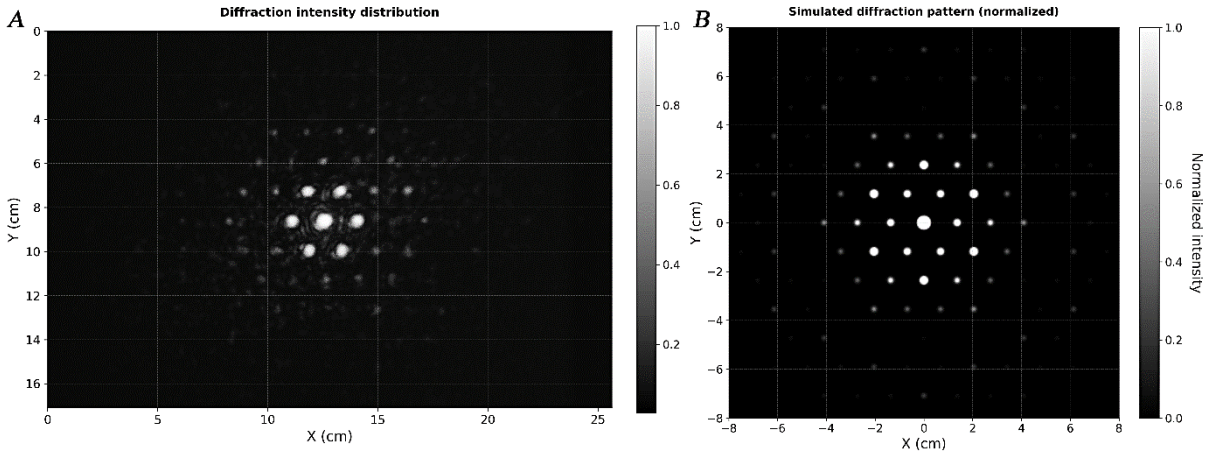

Fig. 7. Diffraction pattern of a honeycomb grating: A – experimental picture on the screen; B – numerical simulation of diffraction for ideal grating geometry ($D = 84$ μm, $a = 169$ μm). Linear normalization and display-only clipping ($I_{sat} = 0.002$) were applied only to the simulated image, following the same procedure as in Figure 1

Source: author's own work

The simulated diffraction pattern (see Figure 7B) is consistent with the experimental result (Figure 7A) in the positions of the diffraction maxima. The pattern exhibits primary bright peaks arranged in a regular hexagonal lattice with inter-peak spacings of $\Delta x \approx 1.36$ cm (horizontal) and $\Delta y \approx 2.37$ cm (vertical). The corresponding experimentally measured values are $\Delta x \approx 1.47$ cm and $\Delta y \approx 2.76$ cm, indicating a systematic increase in the effective lattice spacing observed in the experimental pattern. In addition to the principal diffraction peaks, the experimental image reveals speckle noise (Dainty, 1984) arising from amplitude and phase fluctuations of the incident laser beam.

The real geometry of the fabricated mask was analyzed using optical microscopy (Appendix A, Figure A1e) and ImageJ. Accurate determination of disk diameters is complicated by the presence of local bridging ("connective bridges") between adjacent disks due to toner spreading, leading to partial thickening and extended opaque regions. As a result, many areas form interconnected structures spanning several disks (typically 2–4), while preserving the overall honeycomb topology.

The characteristic size of opaque regions associated with lattice sites is $D = 120.0 \pm 19.6$ μm (+43 % ± 23 % relative to the nominal value of 84 μm).

Thick interconnections between neighboring features prevented reliable automated detection; the nearest-neighbor distance was therefore measured manually. The nearest-neighbor distance (lattice parameter a), measured over 18 pairs in three hexagonal cells, is $a = 182.1 \pm 21.8$ μm, corresponding to a deviation of +7.8 % from the nominal value and a relative uncertainty of about 12 %.

Despite these fabrication-induced distortions, the structure retains long-range order, albeit in a weakened form, as evidenced by the clear hexagonal symmetry of the diffraction pattern. The primary diffraction maxima positions remain largely unchanged, governed by the average lattice periodicity, while local geometric distortions primarily affect intensity and peak sharpness.

6. Fraunhofer diffraction by a random array of disks (Poisson point process). In this subsection, we present an experimental visualization of Fraunhofer diffraction produced by an amplitude mask consisting of identical opaque disks whose centers were first digitally generated according to a Poisson point process (PPP) (Kingman, 1992). The designed mask contained disks of nominal diameter D = 84 μm, distributed over an active area of about 183 × 254 mm^2, yielding a target filling factor of η ≈ 33 %.

The experimental mask was then fabricated by laser printing on A4-format transparent film. Optical microscopy and subsequent image analysis using ImageJ revealed that toner spreading and local merging produced deviations from the nominal design. Two representative regions were examined: (i) areas with relatively well-defined disks and (ii) regions exhibiting pronounced toner-related artefacts, typically occurring in zones of higher local disk density.

In the region with comparatively clean disk formation (Appendix A, Figure A1f), 22 individual disks were identified along with several aggregated features formed by partial overlap of neighboring disks. The average equivalent diameter of disks was D = 109.5 ± 13.6 μm, corresponding to an increase of approximately 30.4 % relative to the nominal diameter. Elongated and oval-shaped structures were also observed, originating from the merging of closely spaced elements.

In contrast, in regions with higher disk density (Appendix A, Figure A1g), printing artefacts become dominant. The disks lose circular symmetry and exhibit irregular, jagged, and asymmetric shapes with blurred and partially discontinuous boundaries. A diffuse halo is observed around many features due to toner spreading, accompanied by randomly distributed fine particles (typically 5–10 μm in size). In such regions, the toner forms complex aggregated structures rather than well-defined individual disks. This behavior is attributed to non-uniform toner transfer and particle aggregation during the thermal fixation stage of laser printing, and it significantly alters the effective amplitude mask structure.

To interpret the experimental results, two numerical simulations of Fraunhofer diffraction were performed using a reduced computational domain. In both cases, 1390 disks were generated within an area of 5.0 × 5.0 mm^2, with their centers distributed according to a Poisson point process.

In Scenario A, all disks were assigned the effective diameter D = 109 μm, corresponding to the experimentally measured value.

In Scenario B, the disk diameter was likewise set to D = 109 μm; however, additional fabrication-induced distortions were introduced to account for deviations from ideal geometry. Specifically, disk edges were randomly perturbed with a roughness of 15% of the radius and a phase distortion amplitude of 0.3 radians, applied in a random manner along the perimeter of each disk. In both scenarios, a Gaussian edge smoothing with σ = 1.5 pixels (on a 4096 × 4096 computational grid) was applied to model the finite resolution of the printing process.

A comparison between the experimental diffraction pattern and the numerical simulations is presented in Figure 8.

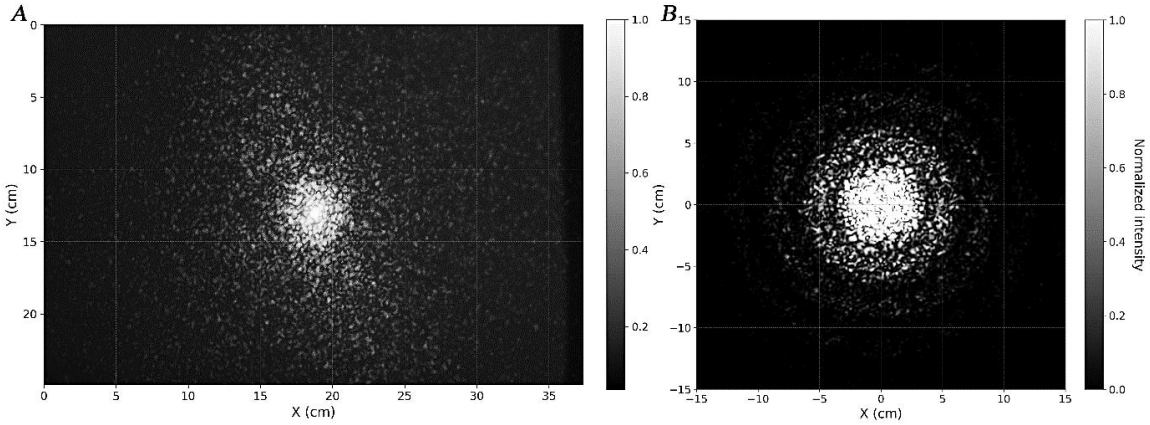

Fig. 8. Comparison of Fraunhofer diffraction patterns for a Poisson-distributed array of disks: A – experimental diffraction pattern; B – numerical simulation for monodisperse disks (D = 109 μm) with nonlinear tone mapping (exposure = 1.5, γ = 1.5) applied to enhance weak diffraction rings (for visualization only)

Source: author's own work

The experimental diffraction pattern (Figure 8A) is characterized by a pronounced central maximum. The first minimum of the diffraction envelope, expected at a radial distance of approximately r_1 ≈ 3.9 cm (corresponding to an effective disk diameter of about 109 μm), is only weakly discernible, and higher-order rings are largely suppressed. In contrast, the numerical simulation for monodisperse disks with D = 109 μm (Figure 8B) exhibits a well-defined diffraction pattern, where not only the first minimum but also higher-order diffraction rings are clearly visible, reflecting the single-particle diffraction envelope expected for an ensemble of opaque disks with uncorrelated spatial positions, in accordance with the array theorem of statistical optics (Goodman, 1996; Singh, 2023).

When fabrication-induced distortions are incorporated (Figure 9), including irregular disk contours and random phase variations, the first minimum becomes barely discernible, and higher-order rings effectively disappear, bringing the simulated pattern into close agreement with the experimental observation. This comparison is qualitative and based on the visibility of structural features only.

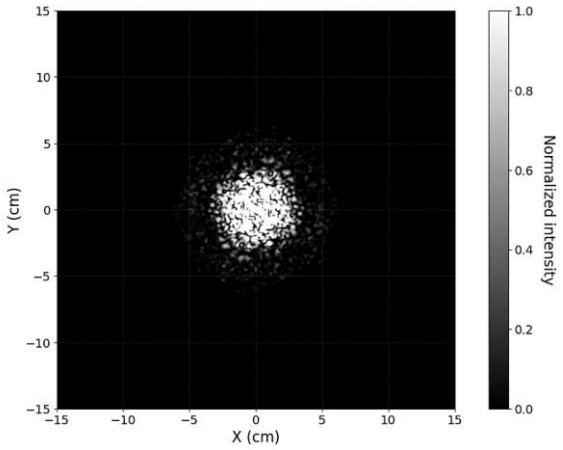

Fig. 9. Numerical simulation of Fraunhofer diffraction for a Poisson-distributed array of disks including fabrication-induced effects such as edge roughness, contour modulation, and random phase distortions (*D* = 109 µm). Nonlinear tone mapping was applied as described in Figure 8 for visualization purposes

Source: author's own work

Additional printing defects occurring in regions of overlapping disks, such as microbubbles and toner microparticles, further increase the heterogeneity of the effective transmission function, enhancing the superposition of non-identical contributions from individual mask elements. This leads to a strong suppression of the visibility of diffraction rings. Consequently, the experimental pattern is dominated by a central maximum surrounded by a diffuse, speckle-like halo.

In a teaching context, this example clearly illustrates how deviations from an idealized ensemble of uncorrelated disk positions – in particular overlap, irregular disk shapes, and local inhomogeneities – lead to a progressive loss of contrast in diffraction patterns, ultimately obscuring the features predicted by the idealized model.

7. Diffraction by disordered disk distributions with a minimal inter-disk distance (Poisson Disk Sampling). In this subsection, we present an experimental realization of a two-dimensional amplitude mask in which identical disks are distributed according to a Poisson disk sampling (PDS) scheme (Bridson, 2007). In contrast to a purely random (PPP) distribution, this configuration imposes a minimum center-to-center distance between disks, preventing clustering and large voids. As a result, the diffraction pattern becomes more regular.

The digital mask was designed with disks of nominal diameter D = 84 µm and a minimum center-to-center distance d_{min} = 169 µm, corresponding to a calculated filling factor of $\eta \approx 12.5$ %. The corresponding physical mask was fabricated by laser printing on a transparent A4 sheet with a resolution of 1200 dpi, including unprinted margin regions.

Microscopic analysis of the printed mask (Appendix A, Figure A1h) revealed significant deviations from the nominal design geometry. Within the analyzed area ($\sim 2.9 \times 10^6$ µm^2), 33 disks were identified, including two instances of merged neighboring disks, which were excluded from the statistical analysis. Around each disk, local inhomogeneities in toner density are observed, forming a diffuse halo of approximately 5–9 µm in width.

Using ImageJ, the average equivalent disk diameter was determined as D = 117.6 ± 12.1 µm, which corresponds to an increase of approximately 40 % ± 14 % relative to the nominal value of 84 µm. A significant size dispersion is observed, indicating pronounced polydispersity of the disks. Deviations from circularity (aspect ratio AR = 1.1 ± 0.1) have a comparatively minor effect.

In addition, the nearest-neighbor distances between disk centers were analyzed. The minimum measured value was 170.0 µm, which differs from the nominal value d_{min} = 169 µm by less than 1 %, confirming that the imposed spacing constraint is well preserved in the printed structure. The average nearest-neighbor distance was found to be 206.7 ± 30.0 µm.

The experimental Fraunhofer diffraction pattern, recorded on a screen, is shown in Figure 10A. The pattern is characterized by a pronounced central maximum with high circular symmetry and a clearly visible first diffraction ring. The radial position of the first minimum is consistent with the average effective disk diameter, as expected from Babinet's principle for complementary apertures. This behavior can be understood as follows: the observed intensity is interpreted as an effective (ensemble-averaged) superposition of diffraction patterns produced by disks of different diameters. Since the angular position of the first minimum scales approximately as $\theta \propto 1/D$, the experimentally observed size dispersion results primarily in a slight radial broadening of the minimum rather than a systematic shift of its mean position. In contrast, higher-order rings, which are more sensitive to diameter variations and phase differences, are strongly suppressed due to averaging over the size distribution. The fine-scale granular intensity background (speckle-like intensity fluctuations) observed in the diffraction pattern arises from the disordered PDS distribution, combined with structural imperfections and local printing inhomogeneities. Nevertheless, the overall shape of the central maximum is primarily governed by the average effective disk diameter across the ensemble.

It should be noted that the additional distortions introduced in subsection 3.6 – namely enhanced edge roughness and random phase modulation – were deliberately not applied in the simulations presented in this and subsequent subsections. In the case of a purely Poisson distribution with significant disk overlap, these effects are essential to reproduce the pronounced weakening of the diffraction ring structure observed experimentally. In contrast, when a minimum inter-disk distance is imposed, spatial correlations alone are sufficient to stabilize the diffraction pattern and preserve well-defined ring features. Moreover, as demonstrated in previous studies (Kathavate, 1945; Li et al., 2009), increasing the local disk density in such correlated arrangements can further enhance the contrast of diffraction rings.

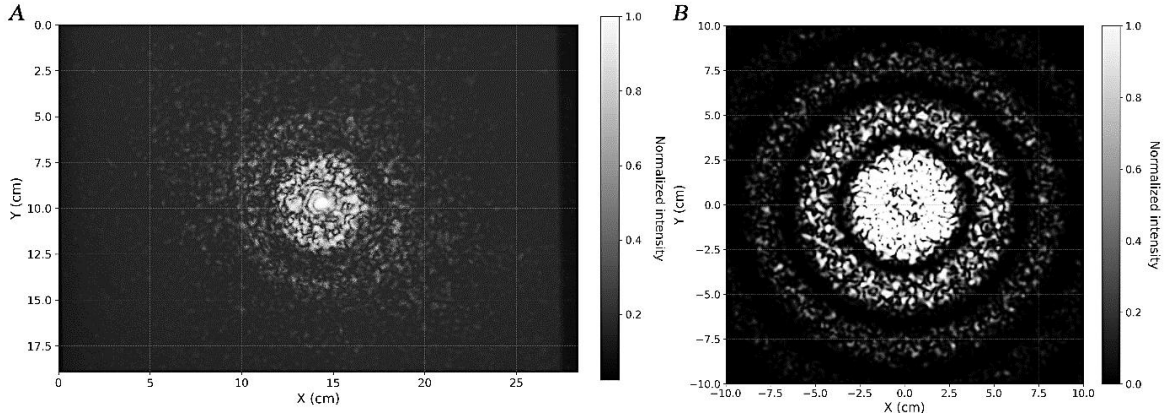

Fig. 10. Comparison of diffraction patterns: A – experimental pattern recorded on the screen; B – simulation of Fraunhofer diffraction for monodisperse disks (D = 117 µm, d_{min} = 169 µm). Nonlinear tone mapping was applied only to the simulation results using the same parameters as in Figure 8, for visualization purposes

Source: author's own work

A numerical simulation was performed using a PDS distribution with parameters corresponding to the experimentally measured average geometry (Figure 10B), while assuming a monodisperse disk ensemble (D = 117 µm, d_{min} = 169 µm, PDS, η ≈ 24 %). Compared to the nominal disk diameter of 84 µm, the increased effective size leads to a smaller radius of the first diffraction minimum (r_1 ≈ 3.6 cm), in agreement with the experimental observation (r_1 ≈ 3.5 cm).

An additional numerical simulation was performed incorporating disk size polydispersity consistent with the experimentally measured distribution. In this model, disk diameters were randomly sampled from a normal distribution with mean D = 117 µm and standard deviation σ = 12 µm, while preserving the same PDS spatial arrangement.

The resulting diffraction pattern is shown in Figure 11. In contrast to the monodisperse case, where multiple diffraction rings are clearly visible, the inclusion of size polydispersity leads to a substantial suppression of higher-order rings. The diffraction pattern becomes dominated by a pronounced central maximum and a single broad first ring, in close agreement with the experimental observation.

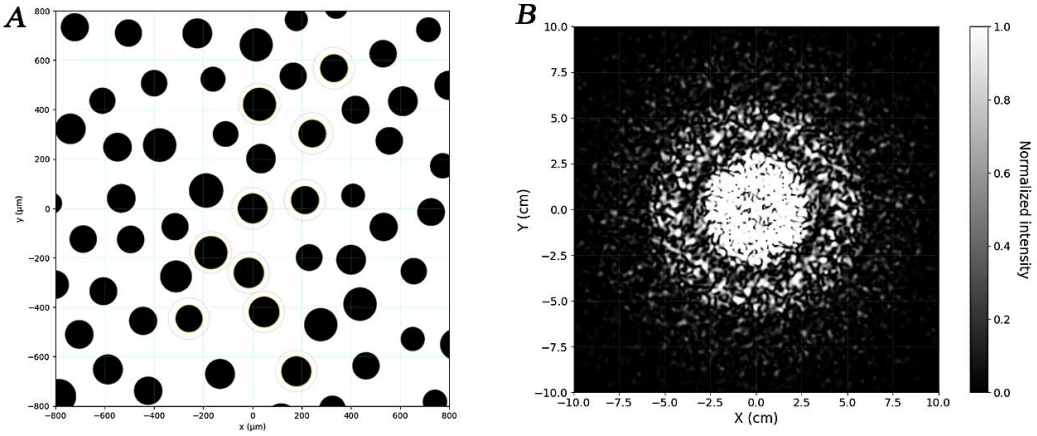

Fig. 11. Poisson Disk Sampling distribution with disk size polydispersity (D = 117 ± 12 µm, d_{min} = 169 µm): A – amplitude mask; B – simulated Fraunhofer diffraction pattern. Nonlinear tone mapping was applied only to the simulation results using the same parameters as in Figure 8, for visualization purposes

Source: author's own work

The comparison demonstrates that disk size polydispersity is the dominant factor governing the reduction of ring visibility in the experimental diffraction pattern, whereas other imperfections (such as shape distortions and local toner inhomogeneities) play a secondary role.

From an educational perspective, this example clearly demonstrates how the interplay of minimal spacing, disk polydispersity, and local printing inhomogeneities affects the formation and visibility of diffraction features. It provides a concrete illustration of how ideal theoretical predictions are progressively modified under realistic experimental conditions. Students can explore these effects directly by varying disk spacing or simulating different levels of polydispersity and edge roughness, observing the resulting changes in the diffraction pattern. This hands-on approach reinforces the link between object geometry and Fraunhofer diffraction, highlighting the sensitivity of patterns to structural imperfections and making PDS masks a valuable tool for teaching fundamental wave optics concepts.

8. Diffraction by a disordered array of randomly oriented square elements (Poisson Disk Sampling). In this subsection, we present numerical simulation of Fraunhofer diffraction from a two-dimensional disordered structure composed of square opaque elements of fixed size. The centers of the squares are distributed using the Poisson Disk Sampling (PDS) method, which

enforces a minimum center-to-center distance and produces a spatially uniform pseudorandom arrangement without clustering or large voids. Each square is independently rotated by a random angle in the range 0^0–360^0, resulting in an ensemble with completely uncorrelated orientations.

Due to practical limitations of laser printing – such as anisotropic toner spreading and orientation-dependent edge distortions – this configuration is considered here exclusively within numerical simulation.

A square aperture produces a diffraction pattern described by a separable sinc^2 function, which is inherently anisotropic. However, when a large number of such elements with random orientations are superimposed, the resulting intensity distribution becomes statistically isotropic. As a result, the far-field diffraction pattern exhibits concentric ring-like structures despite the absence of any long-range positional order (Khachatrian et al., 2025).

In the simulation, a 5.0 × 5.0 mm^2 area contains 495 square elements with side length a = 104 μm and a minimum center-to-center distance d_{min} =180 μm, corresponding to a filling factor of η ≈ 21.0 %. The ratio d_{min}/a ≈ 1.73 ensures moderate packing density while preserving spatial uniformity.

Figure 12 shows generated mask and the corresponding diffraction pattern.

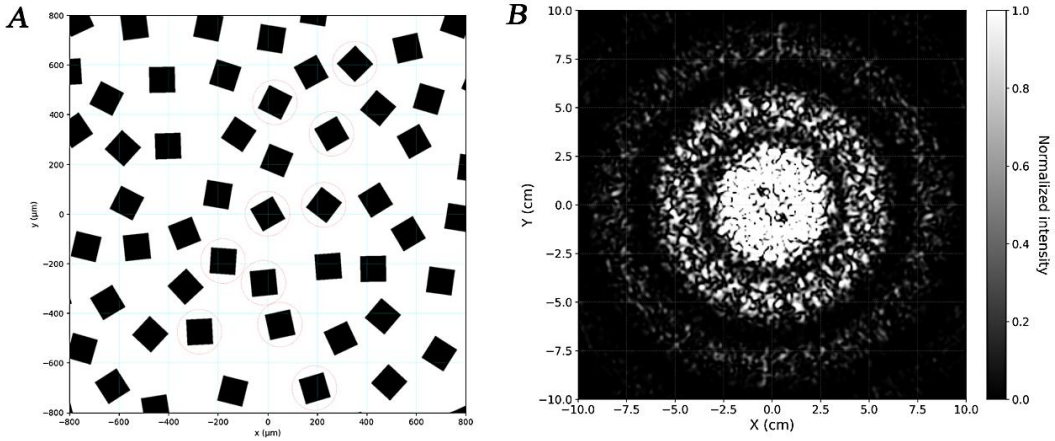

Fig. 12. Poisson Disk Sampling distribution of square elements (a = 104 μm, d_{min} = 180 μm, η ≈ 21.0 %): A – amplitude mask; B – simulated Fraunhofer diffraction pattern. Nonlinear tone mapping was applied as described in Figure 8 for visualization purposes

Source: author's own work

The characteristic radial scale of the diffraction pattern is governed by the size of individual elements. For a square aperture, the first zeros of the diffraction pattern occur at angles $\theta_x = \theta_y \approx \lambda/a$ along the principal axes. In the case of randomly oriented squares, these anisotropic features average out, giving rise to an effective circular minimum at a radial distance of approximately r ≈ 3.3 cm for a = 104 μm, λ = 0.532 μm, and z = 6.5 m.

This example demonstrates that even strongly anisotropic individual scatterers can produce an isotropic diffraction pattern when their orientations are randomized. It highlights the distinction between the form factor of individual elements and the statistical properties of their spatial distribution, providing a useful conceptual illustration for understanding diffraction in disordered systems. Students can extend this approach by simulating various element shapes – triangles, stars, rectangles – within similar pseudorandom distributions to explore how object geometry influences the resulting diffraction patterns.

9. Diffraction by a Poisson–Voronoi disk structure with suppressed long-wavelength fluctuations. In contrast to the classical PDS, which enforces a minimum distance between centers and thereby suppresses only short-wavelength density fluctuations, hyperuniform structures additionally suppress long-wavelength (low-frequency) fluctuations**,** enhancing statistical uniformity on large scales. To approximate such a state, a two-stage method is employed, combining initial PDS placement with modified Voronoi relaxation.

The initial configuration of disk centers was generated using the standard PDS (D=84 μm, d_{min}=169 μm) and used as input for three iterations of Lloyd's relaxation (Lloyd, 1982). During relaxation, Voronoi cells (Du et al., 1999) intersecting the domain boundary (unbounded cells) were excluded from centroid recalculation, and any centroids falling outside the working area were discarded. We denote this combined procedure as Poisson–Voronoi Relaxation with Boundary Suppression (PV-RBS), ensuring that only interior points contribute to the redistribution, thereby enhancing local uniformity while suppressing boundary-induced artifacts. The digital mask was generated for an A4 transparent film with margins.

Direct inspection of the printed mask (Appendix A, Figure A1i, showing a representative fragment of the analyzed region) using ImageJ shows that within the analyzed area (~2.9 × 10^6 μm^2), 45 disks were identified. As in previous cases, a diffuse halo is observed along the disk boundaries. The measured aspect ratio AR = 1.1 ± 0.1 indicates slight deviations from circularity, while the disk diameters are D = 127.9 ± 10.6 μm (≈ 52 % ± 13 % relative to the nominal 84 μm), significantly exceeding the nominal value due to toner spreading. The minimum nearest-neighbor center-to-center distance was estimated as a = 183.4 ± 6.6 μm in the analyzed image.

Small variations in disk sizes introduced by the printing process cause the observed diffraction pattern to represent a superposition of slightly different diffraction patterns, reducing the sharpness and contrast of higher-order rings. However, a notable feature of this configuration is the presence of a narrow dark correlation-induced ring within the central maximum.

For diffraction simulation, a 5.0 × 5.0 mm^2 mask was generated using the experimentally measured PV-RBS parameters (D ≈ 128 μm, d_{min} ≈ 183 μm).

Figure 13 shows a comparison of the experimental pattern on the screen and the numerical simulation of Fraunhofer diffraction. In the simulation, a monodisperse disk ensemble was assumed (i.e., without size polydispersity), using a uniform disk diameter D ≈ 128 μm. As shown in Figure 13B, the central diffraction maximum retains nearly ideal circular symmetry and, in terms of its characteristic size, is consistent with the diffraction envelope corresponding to an effective diameter close to the measured value. Modeling the disks as a monodisperse ensemble results in well-defined diffraction rings in the simulated pattern, together with a narrow dark ring within the central maximum.

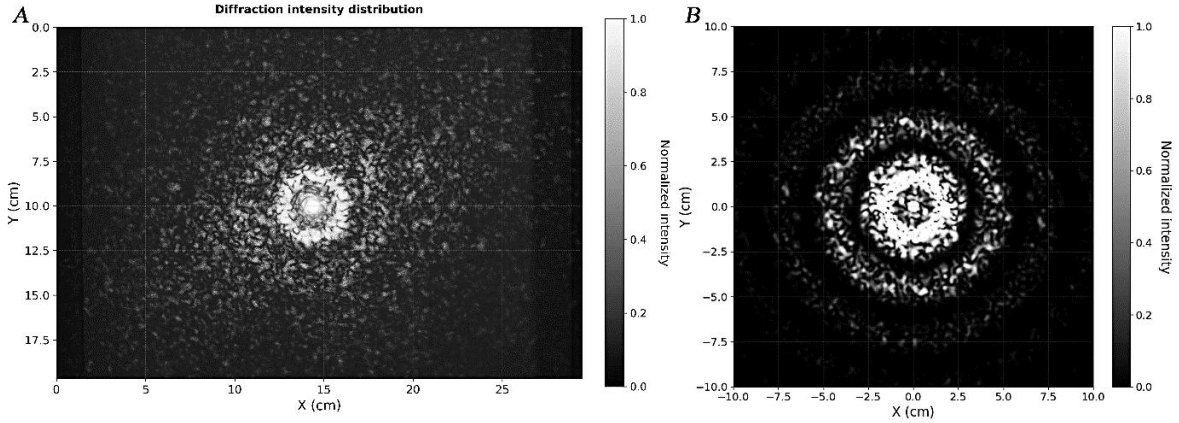

Fig. 13. Comparison of diffraction patterns: A – experimental pattern on the screen; B – numerical simulation of Fraunhofer diffraction using the experimentally measured parameters. Nonlinear tone mapping was applied only to the simulated image for visualization purposes, following the same procedure as in Figure 8 but with a different percentile threshold to enhance the visual contrast in the central region of the pattern

Source: author's own work

The narrow dark ring, extending from approximately 4 mm to 14 mm from the central maximum (see Figure 13A), provides a clear visual indication of suppressed long-wavelength density fluctuations (approximate hyperuniformity). The first diffraction minimum is located at approximately 3.3 cm, consistent with an effective disk diameter of D ≈ 128 μm.

This configuration provides a clear demonstration of correlation-induced features in a format suitable for laser printing. The resulting diffraction patterns are easily accessible for classroom or laboratory observation, enabling students to explore the influence of suppressed long-wavelength fluctuations on diffraction. Such visualizations offer a practical and intuitive way to connect theoretical concepts with observable optical phenomena.

10. Analogy with laser diffraction on spherical microparticles. The opaque microstructures considered in this work, in particular ensembles of disks, provide a clear optical analogue of diffraction and scattering by three-dimensional spherical microparticles. In the Fraunhofer regime, the scattering amplitude of an individual object is governed primarily by its projection onto the plane perpendicular to the incident beam. For particles whose characteristic dimensions are much larger than the wavelength, the diffraction pattern is therefore determined mainly by the geometric shadow of the object.

In this limit, the projection of an opaque or absorbing sphere of radius (R_{sp}) is equivalent to a circular disk of the same radius, which – according to Babinet's principle – is in turn equivalent to a circular aperture. Its diffraction pattern consists of a series of concentric rings, whose far-field intensities are described by (Fischbach & Bond, 1984):

$$I(\theta) \propto \left[\frac{2J_1\left(\frac{2\pi}{\lambda}R_{sp}\sin\theta\right)}{\frac{2\pi}{\lambda}R_{sp}\sin\theta}\right]^2, \quad (10)$$

where J_1 is Bessel function of the first kind and θ is the scattering angle. This expression coincides with the Fraunhofer diffraction result for an opaque circular disk of radius R_{sp}, obtained as the Fourier transform of a circular aperture. Within this approximation, the printed opaque disks used in the present work act as two-dimensional optical analogues of spherical scatterers**.**

However, for ensembles of identical particles, the observed diffraction pattern is not determined solely by the form factor of an individual element. Within the kinematic approximation commonly employed in wave-scattering theory, the total far-field intensity can be expressed as the product of the single-particle form factor and the ensemble structure factor (Feigin & Svergun, 1987; Guinier & Fournet, 1955). The form factor defines the overall envelope of the diffraction intensity, whereas the structure factor reflects spatial correlations between particle positions and governs the redistribution of intensity within this envelope**.**

This distinction becomes particularly evident when comparing ordered and disordered arrangements of identical disks (or, by analogy, spherical microparticles). Long-range order selects discrete diffraction directions associated with reciprocal-lattice vectors, whereas the absence of long-range order leads to an isotropic redistribution of scattered intensity. For disordered ensembles, such as Poisson point processes or configurations generated by Poisson disk sampling, the diffraction pattern is radially symmetric, and the contribution of the single-disk form factor manifests itself as concentric rings analogous to Airy rings.

In contrast, for periodic ensembles of disks arranged in square, centered square, or hexagonal lattices, continuous rings are not observed. Instead, diffraction intensity appears at discrete points in reciprocal space, whose positions are fixed by the

lattice geometry. The resulting diffraction pattern consists of a regular array of narrow maxima modulated by an envelope determined by the single-disk form factor, with only those reciprocal-lattice nodes lying within the region of significant form-factor amplitude being observable.

For particles of noncircular shape, such as opaque squares or rectangles, the single-element form factor becomes intrinsically anisotropic and is described by direction-dependent sinc-type functions. In periodic lattices of such elements, this anisotropy gives rise to direction-dependent diffraction intensities and selection rules. At the same time, for randomly oriented or statistically isotropic ensembles of noncircular elements, the anisotropic contributions of individual elements are effectively averaged out, and the resulting diffraction pattern again approaches radial symmetry despite the noncircular shape of the particles.

Thus, the binary amplitude masks proposed in this work enable a clear separation between the effects of individual particle shape (form factor) and spatial organization of the ensemble (structure factor). This separation represents a central concept in diffraction and scattering theory and provides a transparent educational framework for relating real-space microstructure to characteristic features of diffraction patterns in reciprocal space.

11. Educational analogies with X-ray Diffraction. The Fraunhofer laser diffraction patterns obtained from printed amplitude microstructures provide clear optical analogies of X-ray diffraction and scattering in crystalline, polycrystalline, amorphous, and correlated disordered materials.

Optical masks employed in the present work represent two-dimensional projections of the scattering density and therefore correspond to two-dimensional sections of reciprocal space, rather than full three-dimensional powder diffraction patterns. Consequently, the presented analogies are most directly related to Laue diffraction, two-dimensional scattering experiments, and planar sections commonly encountered in X-ray diffraction and small-angle X-ray scattering (SAXS). Within this well-defined limitation, the correspondence between optical and X-ray diffraction remains robust and instructive.

The transition from perfectly ordered lattices to disordered ensembles is particularly illustrative from a pedagogical perspective. Periodic microstructures produce discrete Bragg-like maxima that reflect lattice symmetry and basis effects, whereas disordered and partially ordered structures give rise to diffuse scattering, concentric rings, and correlation-induced features. These optical diffraction patterns provide direct qualitative analogies to powder X-ray diffraction and SAXS from disordered materials.

A qualitative summary of these optical diffraction analogies is provided in Appendix B (see table B1).

CONCLUSIONS AND PERSPECTIVES FOR A FURTHER RESEARCH

The integrated method developed in this work combines numerical simulations based on the two-dimensional fast Fourier transform with simple experimental visualizations of Fraunhofer diffraction using binary amplitude masks printed on transparent film and illuminated by a low-cost semiconductor laser pointer ($\lambda = 0.532$ μm). This approach provides a coherent and visually intuitive framework for teaching a wide spectrum of spatial arrangements – from perfectly periodic lattices (discrete Bragg peaks) through Poisson-distributed and Poisson-disk-sampled ensembles (isotropic speckle and diffraction rings) to hyperuniform-like structures (characteristic dark correlation ring) – and establishes direct optical analogies with X-ray Laue diffraction and small-angle scattering. Experimental diffraction patterns are complemented by numerical simulations, providing a more complete representation of diffraction from opaque disks.

The comparison is restricted to the spatial distribution of diffraction features, while absolute intensity values are not used as a metric of agreement.

From an educational perspective, the method is particularly powerful. Students can independently design masks of arbitrary complexity, print them on a standard office laser printer, observe the resulting far-field patterns on a screen, and directly compare them with numerical simulations. This hands-on workflow makes abstract concepts – Fourier optics, reciprocal space, structure factor, systematic absences, and short- and long-range correlations – tangible and memorable, while demonstrating the deep connection between optical diffraction and X-ray techniques.

At the same time, the laser printer itself embodies the pedagogical duality of the approach. On the one hand, it is an extremely accessible and inexpensive device available in virtually any educational institution. On the other hand, it is not a precision instrument at the microscale. Two main groups of fabrication-induced deviations appear systematically:

- Positioning inaccuracies and local distortions of the pixel grid, which are more pronounced for closely spaced structural elements;
- Toner spreading and halo formation during the fusing process, leading to an increase in the effective size of printed features relative to the nominal value, typically by 20–40%, which in turn is the main source of the observed size polydispersity.

Moreover, the effective size of opaque elements depends on the local pattern geometry: increased spacing tends to enhance toner spreading, whereas dense packing may lead to partial merging of features. In periodic lattices, these effects have only a minor influence on the positions of Bragg peaks in reciprocal space. However, in disordered ensembles, such as Poisson-distributed disks without a minimum inter-disk distance, the diffraction ring structure is highly sensitive: variations in effective disk diameter lead to radial scaling of diffraction rings, while size polydispersity reduces their contrast. At higher filling fractions, feature merging can further disrupt the ring structure, gradually transforming it into a diffuse speckle field. Therefore, when designing masks, it is advisable to deliberately reduce the nominal disk diameters by approximately 20–40% relative to the design values, depending on the specific printer and toner, in order to ensure that the observed diffraction patterns reproduce the predicted spatial features of the simulated patterns.

Importantly, these “imperfections” are not merely drawbacks. They provide a useful teaching opportunity: students learn to distinguish between ideal theoretical predictions and real experimental outcomes, quantify fabrication tolerances, and understand how the same physical limitations affect ordered versus disordered systems differently. This meta-level reflection

reinforces the link between theory, simulation, and experimental realization, one of the central goals of the proposed laboratory practicum.

Despite these practical limitations, the method remains robust, scalable, and highly adaptable. Future work may focus on quantitative analysis of diffraction intensity statistics, providing a more direct link between fabrication imperfections and far-field diffraction features, including speckle contrast, ring visibility, and correlation-induced effects. Higher-resolution printing technologies (2400–4800 dpi) would further enable exploration of finer structural regimes, including fractal, quasi-periodic, and hyperuniform patterns.

Overall, the integrated experimental–numerical framework provides a low-cost and versatile platform for teaching Fourier optics phenomena and bridging theoretical predictions with experimentally accessible realizations.

CONFLICT OF INTEREST

The authors declare no conflict of interest.

FUNDING SOURCES

This research did not receive any specific grant from funding agencies in the public, commercial, or not-for-profit sectors.

DATA AVAILABILITY

The data associated with this study are available in Zenodo under the identifier https://doi.org/10.5281/zenodo.18879679.

USE OF ARTIFICIAL INTELLIGENCE (AI) TOOLS

The Claude tool was used to assist in generating Python scripts or parts of scripts. All outputs were reviewed, tested, and manually corrected by the authors.

ACKNOWLEDGEMENTS

The authors would like to thank Dr Richard Cousins for assistance with microscopy at the Nanoscale and Microscale Research Centre (University of Nottingham, United Kingdom).

REFERENCES (TRANSLATED AND TRANSLITERATED)

1. Cowley, L., Laven, P., & Vollmer, M. (2005). Rings around the sun and moon: Coronae and diffraction. *Physics Education, 40*(1), 51. https://doi.org/10.1088/0031-9120/40/1/004
2. Van Hook, S. J. (2007). Inquiry with laser printer diffraction gratings available to purchase. *The Physics Teacher, 45*(6), 340–343. https://doi.org/10.1119/1.2768688
3. Brady, J. B., & Boardman, S. J. (1995). Introducing mineralogy students to X-ray diffraction through optical diffraction experiments using lasers. *Journal of Geological Education, 43*(5), 471–476. https://doi.org/10.5408/0022-1368-43.5.471
4. Naimi, E. K. (2013). Demonstration of the Bragg diffraction of light by a 2D-photon structure. *Russian Microelectronics, 42*, 512–516. https://doi.org/10.1134/S1063739713080118
5. Huang, D., Timmers, H., Roberts, A., Shivaram, N., & Sandhu, A. S. (2012). A low-cost spatial light modulator for use in undergraduate and graduate optics labs available to purchase. *American Journal of Physics, 80*(3), 211–215. https://doi.org/10.1119/1.3666834
6. Tsutaoka, T., Tokunaga, T., Umeda, T., & Maehara, T. (2014). Observation of the two-dimensional reciprocal lattice by use of lattice grating sheets and a laser pointer. *European Journal of Physics, 35*(5), 055021. https://doi.org/10.1088/0143-0807/35/5/055021
7. Peinado, A., Vidal, J., Escalera, J. C., Lizana, A., Campos, J., & Yzuel, M. (2012). Teaching Fraunhofer diffraction via experimental and simulated images in the laboratory. In *Optics Education and Outreach II* (Vol. 8481, p. 84810D). SPIE. https://doi.org/10.1117/12.943241
8. Torquato, S., & Stillinger, F. H. (2003). Local density fluctuations, hyperuniformity, and order metrics. *Physical Review E, 68*, 041113. https://doi.org/10.1103/PhysRevE.68.041113
9. Torquato, S. (2018). Hyperuniform states of matter. *Physics Reports, 745*, 1–95. https://doi.org/10.1016/j.physrep.2018.03.001
10. Easley, C. J., Benninger, R. K., Shaver, J. H., Head, W. S., & Piston, D. W. (2009). Rapid and inexpensive fabrication of polymeric microfluidic devices via toner transfer masking. *Lab on a Chip, 9*, 1119–1127. https://doi.org/10.1039/B816575K
11. Ghosh, R., Gopalakrishnan, S., Savitha, R., Renganathan, T., & Pushpavanam, S. (2019). Fabrication of laser printed microfluidic paper-based analytical devices (LP-µPADs) for point-of-care applications. *Scientific Reports, 9*, 7896. https://doi.org/10.1038/s41598-019-44455-1
12. Born, M., & Wolf, E. (1999). *Principles of optics: Electromagnetic theory of propagation, interference and diffraction of light* (7th ed.). Cambridge University Press.
13. Hecht, E. (2017). *Optics* (5th ed.). Pearson Education Limited.
14. Guenther, B. D. (2020). *Modern optics simplified*. Oxford University Press.
15. Bertero, M., Boccacci, P., & Pike, E. R. (1985). Particle-size distributions from Fraunhofer diffraction: The singular-value spectrum. *Inverse Problems, 1*(2), 111. https://doi.org/10.1088/0266-5611/1/2/003
16. Schneider, C., Rasband, W., & Eliceiri, K. (2012). NIH Image to ImageJ: 25 years of image analysis. *Nat Methods,* 9, 671–675 .https://doi.org/10.1038/nmeth.2089
17. Siegman, A. E. (1986). *Lasers*. University Science Books.
18. Voronkin, O., & Lushchin, S. (2026). *Fraunhofer diffraction of laser-printed microstructures dataset*. Zenodo. https://doi.org/10.5281/zenodo.18879679
19. Dainty, J. C. (Ed.). (1984). *Laser speckle and related phenomena* (2nd enlarged ed.). Springer-Verlag.
20. Kingman, J. F. C. (1992). *Poisson processes*. Clarendon Press.
21. Goodman, J. W. (1996). *Introduction to Fourier optics* (2nd ed.). McGraw-Hill.

22. Singh, M. (2023). A simple experiment to study the array theorem using Fraunhofer diffraction of a two-dimensional grating. *Physics Education, 58*(4), 045007. https://doi.org/10.1088/1361-6552/acd5a3
23. Bridson, R. (2007). Fast Poisson disk sampling in arbitrary dimensions. In *SIGGRAPH '07: ACM SIGGRAPH Sketches* (p. 22). ACM. https://doi.org/10.1145/1278780.1278807
24. Kathavate, Y. V. (1945). The diffraction of light by an assembly of opaque circular disks. *Proceedings of the Indian Academy of Sciences, 21*, 233–239. https://doi.org/10.1007/BF03049858
25. Li, D., Ke, X. L., Jing, H. M., Ping, C., Zhang, P., & Zhou, J. (2009). *Analysis on the Fraunhofer diffraction of randomly distributed holes* [English translation of title]. (*8*), 35–38. https://dxwl.bnu.edu.cn/EN/Y2009/V28/I8/35
26. Khachatrian, A. Zh., Harutyunyan, S. H., Khachikyan, L. E., Muradyan, T. R., Harutyunyan, G. A., & Aghabekyan, V. N. (2025). The plane wave diffraction on a flat area from randomly orientated rectangular apertures. *Results in Physics, 75*, 108348. https://doi.org/10.1016/j.rinp.2025.108348
27. Lloyd, S. (1982). Least squares quantization in PCM. *IEEE Transactions on Information Theory, 28*(2), 129–137. https://doi.org/10.1109/TIT.1982.1056489
28. Du, Q., Faber, V., & Gunzburger, M. (1999). *Centroidal Voronoi tessellations: Applications and algorithms*. *SIAM Review, 41*(4), 637–676. https://doi.org/10.1137/S0036144599352836
29. Fischbach, F. A., & Bond, J. S. (1984). *Fraunhofer diffraction patterns of microparticles*. *American Journal of Physics, 52*(6), 519–521. https://doi.org/10.1119/1.13862
30. Guinier, A., & Fournet, G. (1955). *Small-angle scattering of X-rays*. New York, NY: Wiley.
31. Feigin, L. A., & Svergun, D. I. (1987). *Structure analysis by small-angle X-ray and neutron scattering*. New York, NY: Plenum Press.

Appendix A

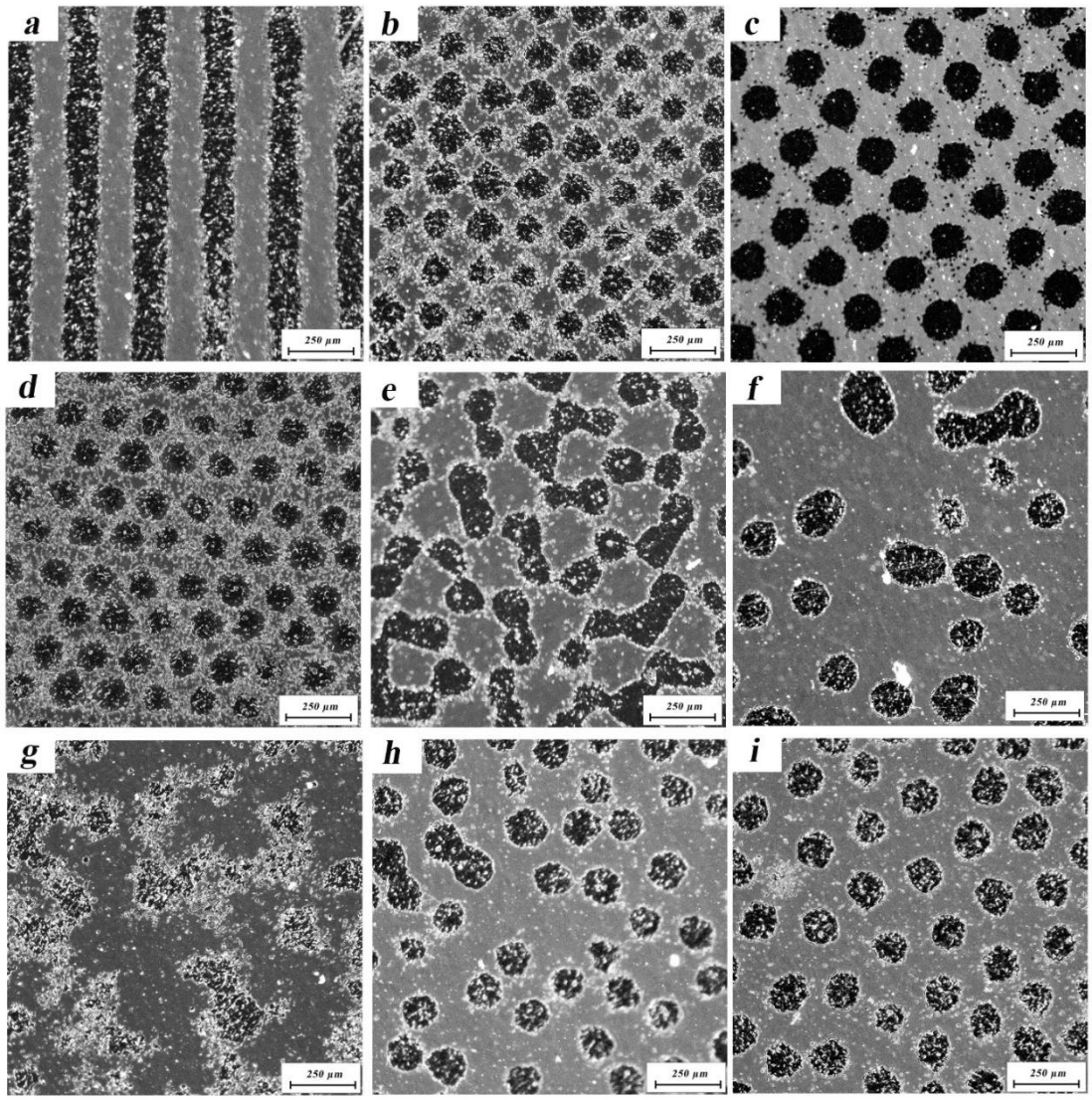

Figure A1. Optical micrographs of fragments from laser-printed A4 masks used in the diffraction experiments (scale bar: 250 μm in all panels). The listed parameters correspond to nominal design values; actual feature sizes vary due to fabrication effects such as broadening, partial merging, or distortion of neighboring elements.
(a) One-dimensional amplitude grating
(b) Two-dimensional periodic grating formed by a regular array of opaque disks

(c) Periodic square grating with additional central disks
(d) Two-dimensional hexagonal grating of opaque disks
(e) Two-dimensional honeycomb grating
(f) Random array of disks (Poisson point process). Sparse region; individual disks and some fused clusters visible.
(g) Random array of disks (Poisson point process). Dense region with irregular toner agglomerates.
(h) Disordered disk distributions with a minimal inter-disk distance (Poisson Disk Sampling)
(i) Disk distribution generated using the PV-RBS algorithm

Appendix B

Table B1. Educational analogies between Fraunhofer laser diffraction patterns and X-ray diffraction and scattering phenomena

№	**Microstructure type**	**Laser diffraction pattern**	**X-ray diffraction / scattering analog**	**Example material or system**
1	One-dimensional grating	Series of discrete maxima aligned along one direction	Laue diffraction from layered or quasi-one-dimensional crystals; line-like reflections	Mica, NaCl viewed along [100]
2	Two-dimensional periodic grating (square lattice of disks)	Square grid of sharp diffraction spots indexed by (m, n)	Laue diffraction from cubic or tetragonal crystals along a principal axis	Si or NaCl in [001] orientation
3	Centered square lattice with a basis (additional disk at the unit-cell center)	Square grid with systematic absences for odd ($m + n$)	Laue diffraction from body-centered cubic lattices; structure-factor extinctions	Fe, W
4	Two-dimensional hexagonal grating of disks	Hexagonal array of Bragg maxima	Laue diffraction from hexagonal crystals	Graphite, ZnO (wurtzite structure)
5	Honeycomb grating (two-site basis on hexagonal grating)	Hexagonal reciprocal lattice modulated by basis-dependent intensity variations	Diffraction from two-dimensional crystals with a multi-atom basis	Graphene, hexagonal BN
6	Random array of disks (Poisson point process)	Bright central maximum with diffuse speckle background, absence of sharp rings	X-ray scattering from amorphous materials and liquids, characterized by diffuse scattering without sharp Bragg peaks	Glasses, liquids
7	Disordered disks with minimum inter-disk distance (Poisson disk sampling)	Central peak accompanied by concentric Airy-like rings due to short-range order	Powder X-ray scattering from nanoparticle ensembles dominated by finite-size effects and short-range correlation	Nanocrystalline metals, colloidal particles
8	Disordered array of randomly oriented square elements (Poisson disk sampling)	Isotropic ring structure modulated by the square-element sinc^2 form factor (azimuthal averaging of anisotropic contributions)	Powder X-ray scattering from randomly oriented anisotropic (plate-like) particles, dominated by the particle form factor	Clay minerals, platelet-like nanoparticles
9	Poisson–Voronoi disk structure with suppressed long-wavelength fluctuations (hyperuniform)	Central maximum containing a dark correlation ring indicating suppressed low-frequency scattering	SAXS signatures of hyperuniform disordered materials with suppressed $S(q \to 0)$	Hyperuniform glasses, jammed packings, disordered photonic solids

| *Received: 15.02.2026* | *Accepted: 30.03.2026* | *Published: 30.04.2026* |